How can the winter North Atlantic Oscillation influence the early summer precipitation in Northeast Asia: effect of the Arctic sea ice

Peng Zhang[1,2,3] · Zhiwei Wu[1,2] · Rui Jin[1,4]

Abstract

The early summer (May–June) precipitation in Northeast Asia (NEA) accounts for about 25% of the annual total, which is important for the local agriculture production. The potential influencing factors and the related mechanisms of early summer NEA precipitation variability, however, are not fully understood. Our study suggests that a dipolar NEA precipitation anomaly pattern in May–June highly resembles the second leading mode of NEA early summer precipitation variability, can be induced by the winter North Atlantic Oscillation (NAO) through the "capacitor" effect of the Barents sea ice (BSI). Further analysis indicated that during negative NAO winter, anomalous northerlies controlling the Barents Sea tend to increase the local sea ice and reach its peak in spring. The BSI anomalies persist from spring to the following early summer generates the "positive–negative–positive" geopotential height anomalies occupying the Arctic, Kamchatka, and extra-tropical western Pacific. The southerlies on the west flank of the anomalous extra-tropical western Pacific anticyclone advect sufficient water vapor from the Pacific to southern NEA, concurrent with lower-troposphere convergence, leading to rich rainfall over Korea and southern Japan. In contrast, the lower-level divergence may reduce the precipitation over northern NEA. At last, a physical-based empirical model is established using the winter NAO index. It shows that the winter NAO provides a promising predictability source for this anomalous NEA dipolar precipitation pattern.

Keywords Barents sea ice · Northeast Asian early summer rainfall · NAO

1 Introduction

The Northeast Asian (NEA) region, which consists of Northeast China, Korea Peninsula, and Japan, is one of the most crowded areas and a key breadbasket in the world. Therefore, as the major crop-growing season, the amount of rainfall in the summer is an important factor in determining the final yield of NEA (Shen et al. 2011; Zhou et al. 2015). Studying the physical process and predicting the year-to-year variability of NEA summer precipitation is of great significance in ensuring food security. Previous studies found the NEA summer rainfall is influenced by ENSO, the tropical Indian Ocean, and tropical Atlantic sea surface temperature (SST) anomalies (Wu et al. 2003; Lee et al. 2005; Gao et al. 2014; Guo and Xiao 2019; Zhao et al. 2020a, b). Except for the tropical factors, the Northeast cold vortex, Arctic dipole, and other circulation anomalies in high latitudes also play important roles (He et al. 2007; Wu et al. 2008; Han et al. 2015).

As the predominant mode of Northern Hemisphere atmospheric variability, the North Atlantic Oscillation (NAO) reflects a seesaw alternation of air mass between Greenland and Azores Island (Wallace and Gutzler 1981; Barnston and Livezey 1987; Hurrell 1995, 1996; Thompson and Wallace 1998, 2000), has been regarded as a multi–timescale atmospheric mode affecting the weather and climate from Eurasia to North America (Brönnimann 2007; Li et al. 2013; Wu and Wu 2019; Feng et al. 2019; Zhang et al. 2019). For boreal spring NAO, a simultaneous

✉ Zhiwei Wu
zhiweiwu@fudan.edu.cn

1 Department of Atmospheric and Oceanic Sciences and Institute of Atmospheric Sciences, Fudan University, Shanghai 200433, China

2 Shanghai Key Laboratory of Meteorology and Health, Shanghai 200030, China

3 State Key Laboratory of Numerical Modeling for Atmospheric Sciences and Geophysical Fluid Dynamics, Institute of Atmospheric Physics, Chinese Academy of Sciences, Beijing 100029, China

4 Shanghai Typhoon Institute, China Meteorological Administration, Shanghai 200030, China

tripolar sea surface temperature (SST) anomalies pattern in the North Atlantic is found to sustain till the following summertime, providing good performance for the seasonal prediction of the southeastern Asia summer rainfall (Wu et al. 2009a, b, 2012a; Zheng et al. 2016). Nevertheless, for Northeast Asia, such preceding NAO-related effects and physical mechanisms are still not clear.

There have also been studies that inspected the effect of winter NAO on the simultaneous Arctic sea ice (Close et al. 2017; Deser et al. 2000; Park et al. 2015; Rothrock and Zhang 2005; Strong et al. 2009; Wu and Wang 2020). Owing to the reduced oceanic and atmospheric heat transport from the Atlantic, the more extensive sea ice, colder seawater, and atmospheric temperature of the Barents Sea are found during the negative phase of NAO/AO (Liu et al. 2004; Wang et al. 2004; Yamamoto et al. 2006; Luo et al. 2017).

As a "cold pole" of the earth, with widespread sea ice, the Arctic presents a notable year-to-year variability and profoundly impacts the local as well as the remote weather and climate (Li and Wu 2012; Guo et al. 2014; Zhang et al. 2018; Yin et al. 2020; Zhang et al. 2020). Accompanied by the rapid diminishing of sea ice in the Arctic during recent decades, more efforts have been made to trace the connection between Arctic sea ice and remote atmospheric anomalies. For example, Screen (2013) attributed the increase of northern European rainfall to the loss of the Arctic sea ice via the southward shift of the summer jet stream over Europe. For East Asia, spring Bering and Okhotsk sea ice might exert great influence on the East Asia precipitation during the subsequent summer through land surface processes and stationary wave activities (Zhao et al. 2004). Applying the singular value decomposition method, Wu et al. (2009a, b) found the anomalous spring Arctic sea ice can trigger a northern Europe-rooted Eurasian wave train that significantly impacts Chinese summer rainfall. He et al. (2018) pointed out that the Silk Road pattern act as an atmospheric bridge connecting Barents sea ice in June and East Asian rainfall anomalies in August. In addition to spring Arctic sea ice, Wu et al. (2013) revealed that via the seasonal persistence of Atlantic SST anomalies, the extensive winter sea ice concentrations west of Greenland can exert its impact on the northern Eurasian climate anomalies in the consequent summer. The below-average autumn sea ice in the Kara-Laptev Sea after the late-1990s may cause the seasonal persistence of soil moisture and snow depth anomalies into the spring, thus feedbacks on the summer precipitation in East Eurasia (Liu et al. 2020).

Having known the connection of NAO and EA summer rainfall, the importance of Arctic sea-ice influence on the EA summer climate as well as their potential linkage with winter NAO, it is justifiable to assume whether the year-to-year variability of the early summer NEA precipitation

can be affected by preceding NAO through the "capacitor" effect of the Arctic sea ice. Two questions will be focused on in this study: (1) Can the NEA precipitation be impacted by the preceding NAO signal? (2) What roles would the Arctic sea ice play? To reply to the above questions, the paper is framed as follows. Section 2 introduces the dataset, methodology, and model. The linkage between winter NAO and NEA early summer precipitation is presented in Sect. 3. Section 4 focuses on the "capacitor" role of Arctic sea ice. A statistic model and some discussions are raised in Sects. 5 and 6.

2 Data, methodology, and model

In this study, the monthly datasets are used including (1) the ERA-interim reanalysis data gridded at 1.5° × 1.5° resolution (Dee et al. 2011); (2) the sea ice concentration (SIC) dataset from Met Office Hadley Centre at 1.0° × 1.0° horizontal resolution (Rayner et al. 2003); (3) the National Oceanic and Atmospheric Administration (NOAA) Extended Reconstructed sea surface temperature Version 5 (ERSST V5) data (Huang et al. 2017); (4) the NOAA's Land Precipitation Reconstruction (PREC/L) data (Chen et al. 2002). (5) monthly station-based NAO index (Hurrell 1995). The data and indices are de-trended before applied to avoid the potential impact of linear trends. The significant tests in this study are based on the student's t-test.

To detect the leading coupling mode between February–March–April (FMA) Arctic sea ice anomalies and May–June (MJ) Northeast Asian precipitation, the singular value decomposition (SVD) analysis (Bretherton et al. 1992) is performed from the covariance between FMA sea ice anomalies in the Arctic region (60° N–90° N, 0°–360°) and rainfall anomalies over Northeast Asia (NEA, 35° N–55° N, 115° E–145° E) in the 39 winters from 1979 through 2017. Regression and composite analysis are also applied. The abnormal years are marked with the absolute values of the normalized index exceed or equal to 0.5. The 8 levels from 1000 to 300 hPa (including 1000, 925, 850, 700, 600, 500, 400, and 300 hPa) are vertically integrated to calculate the water vapor flux.

The 5th generation (version 5.4) the European Center-Hamburg (ECHAM) (Roeckner et al. 2003) atmospheric general circulation model, provided by Max-Plank Institute, is used to illustrate the possible mechanism. In the present study, we use triangular 63 with 19 vertical levels (T63L19) resolutions. Firstly, applying the ECHAM5.4 model, a control experiment forced by AMIP II observed climatology SST with a 30-years integration with the last 20 years' results as the reference. Next, the sensitivity experiments are performed, in which the observational SST and sea ice concentration (SIC) anomalies are added to the early summer

(May–June) climatology SIC and SST with the initial conditions taken from the control experiment and 20 years of integration carried out.

3 NEA early summer rainfall and the winter NAO

Figure 1 presents the climatology precipitation over the NEA. In the early summer (MJ), the average precipitation in Northeast Asia ranges from 100 to 500 mm per-month (Fig. 1a). The range of average annual rainfall is between 300 and 1200 mm per-month (Fig. 1b), indicating the early summer NEA precipitation occupies 20–30% of the annual total (Fig. 1c).

Figure 2a displays the regression map between the DJ NAO index (multiplied by −1) and the early summer rainfall anomalies over Northeast Asia. The result shows that the negative phase of NAO in the preceding winter tends to result in a dipolar rainfall pattern in the NEA during early summer with positive (negative) anomalies over the Korean Peninsula and Japan (the Northeast Asian continent). Based on an empirical orthogonal function (EOF) analysis of the precipitation anomalies in the NEA region (30°–50° N, 115°–145° N), the precipitation leading modes are examined. The first leading EOF mode of early summer precipitation over ENA features a mono-sign pattern with the maximum loading center located over the Korean Peninsula and the southern Japan (not shown). And PC1 accounts for about 32% of the total variance. Figure 2b, c show the spatial–temporal field of the second leading mode. The spatial pattern of EOF2 highly resembles that of Fig. 2a. PC2 accounts for about 15% of the total variance and represents a notable interannual variability. If defining the averaged positive

anomalies (purple box; 35°–39° N, 126°–138° E) minus the averaged negative anomalies (purple box; 41°–48° N, 120°–136° E) as a Northeast Asian dipolar precipitation index (NEADPI), the temporal correlation coefficient (TCC) between MJ NEADPI and PC2 is 0.8, while that between MJ NEADPI and DJ NAO index is −0.54, exceeding the 99% confidence level (Fig. 2c), indicating the opposite-sign precipitation anomalies may appear over the northern and southern NEA continent in the post-NAO early summer. The TCC between PC1 and MJ NEADPI is 0.36, which is much less than that of PC2. Therefore, the anomalous dipolar precipitation pattern reflects the second leading mode of MJ precipitation in the NEA.

Figure 3 compares the composite fields of atmospheric circulation between high and low MJ NEADP indices and between low and high DJ NAO indices. For NEADPI, an obvious anomalous positive–negative–positive geopotential height pattern controls the Arctic, Eurasia, and extratropical western Pacific (XWP). Specifically, a large range of salient positive 850-hPa geopotential (Z850) anomalies is occupying the Arctic. Meanwhile, the salient negative and positive Z850 anomalies control eastern Siberia and XWP, respectively (Fig. 3a). Corresponding to such an abnormal pattern, an anomalous cyclonic (anticyclonic) 500-hPa horizontal wind (UV500) is centered over Kamchatka (southern Japan) and less (more) water vapor is advected to northern NEA (Korea and Japan) from the western Pacific through the southern flank of the cyclone (anticyclone) (Fig. 3c). For NAOI, the corresponding Z850, UV500 (Fig. 3b) and vertically integrated water vapor flux (Fig. 3d) anomalies share similar characteristics with those of NEADPI.

As an internal variability of the atmosphere (Branstator 2002), the NAO seems to be unlikely to persist from winter to the following season. Shukla (1998) has pointed
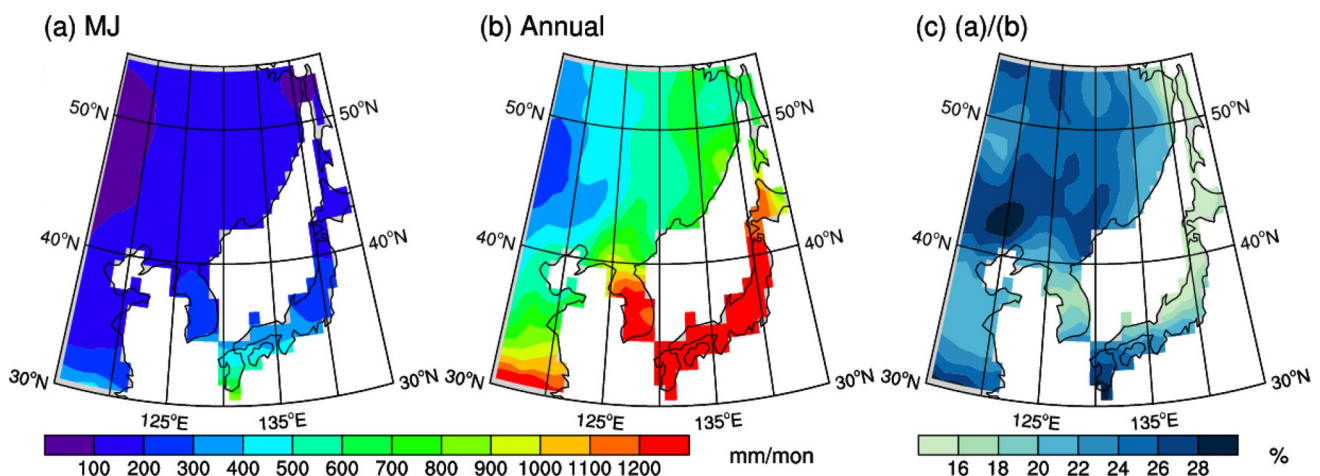

Fig. 1 May–June (MJ) (**a**) and annual **b** mean precipitation (color shadings in units of mm/month, interval: 100 mm/month) in the Northeast Asia (NEA) region, **c** the ratio of **a** and **b** (color shadings in units of %, interval: 2%)
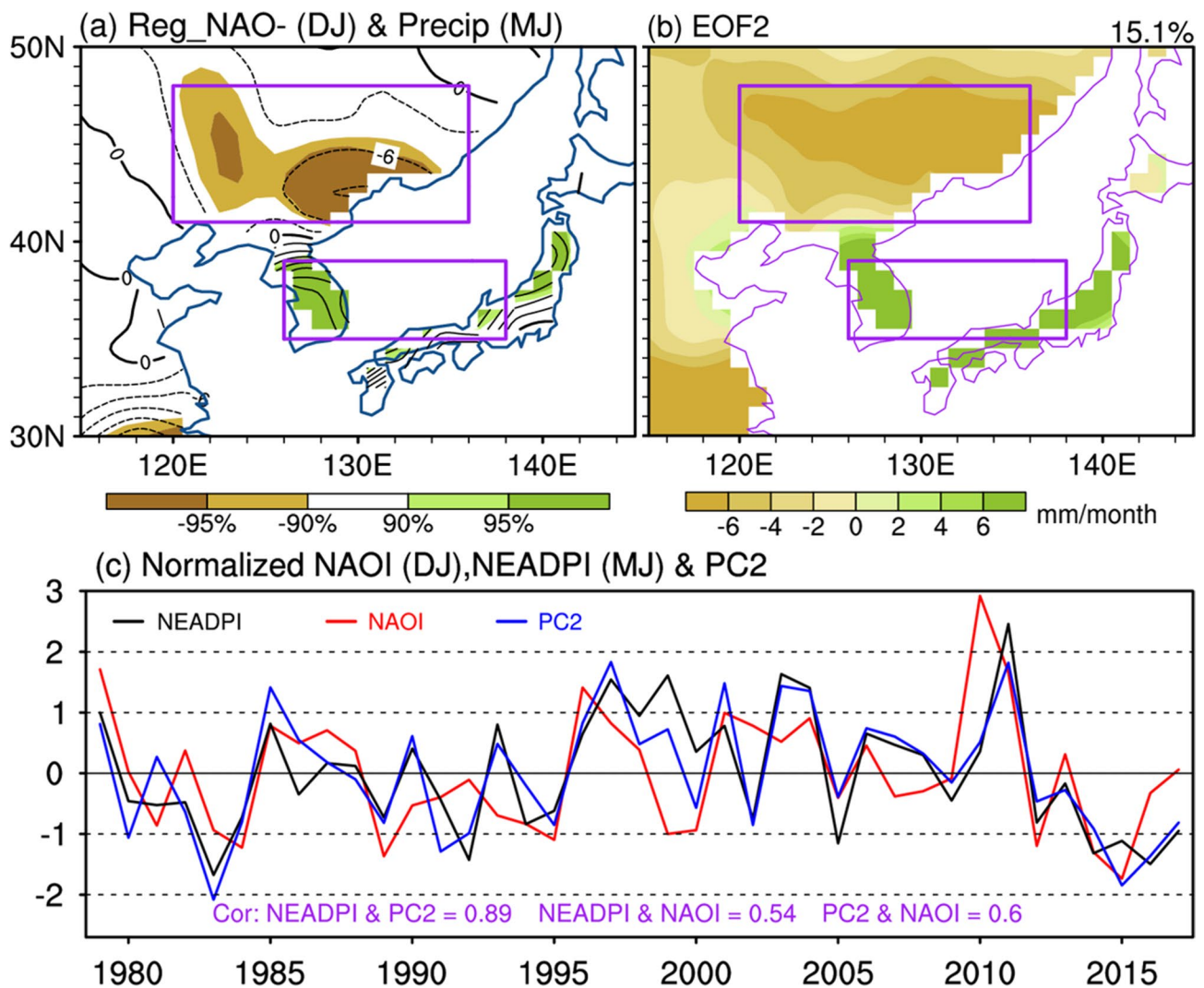
Fig. 2 **a** Linear regression of MJ precipitation (color shadings in units of mm/month, interval: 2 mm/month) anomalies against the DJ North Atlantic Oscillation (NAO, multiplied by −1) index, **b** the second EOF mode of the MJ NEA precipitation. The dark (light) shadings indicate significant values at the 95% (90%) confidence level. Purple boxes indicate the northern (41°–48° N, 120°–136° E) and southern (35°–39° N, 126°–138° E) NEA regions. **c** Time series of the normalized MJ NEA dipolar precipitation (black curve, NEADP), DJ NAO (red curve) indices, and PC2 (blue curve) for the period of 1979–2017

out that the low boundary forcing can store and sustain the anomalous atmospheric signal and then impact the regional climates in the subsequent months. The low boundary conditions associated with winter NAO, therefore, should be taken into accounts to examine their potential roles. Previous studies have found that the tripolar SSTA associated with strong NAO can generate wave trains that further impact the EA summer monsoon (Wu et al. 2009a, b; Zuo et al. 2013). Thus, we examine the composite difference of MJ SST over the North Atlantic (NA) between low and high DJ NAO years. It shows that after a winter NAO reaches the extreme negative phase, a distinct tripolar SSTA pattern would appear over NA in the following summer (Fig. 4a). A NA tripolar SSTA index (NATI, Fig. 4b) is calculated

using the sum of averaged positive SSTAs in the tropical (6°–22° N, 20°–60° W) and extra-tropical (56°–68° N, 10°–60° W) Atlantic minus the averaged negative SSTA in the mid-latitude (38°–46° N, 30°–50° W) Atlantic. The TCC between this NATI and MJ NEADPI is 0.26, not reaching the significant level ($p < 0.1$) based on the Student's t-test. Considering the NAT SSTA may not be the key factor connecting the DJ NAO and MJ NEADP, other low boundary factors are needed to be further inspected.
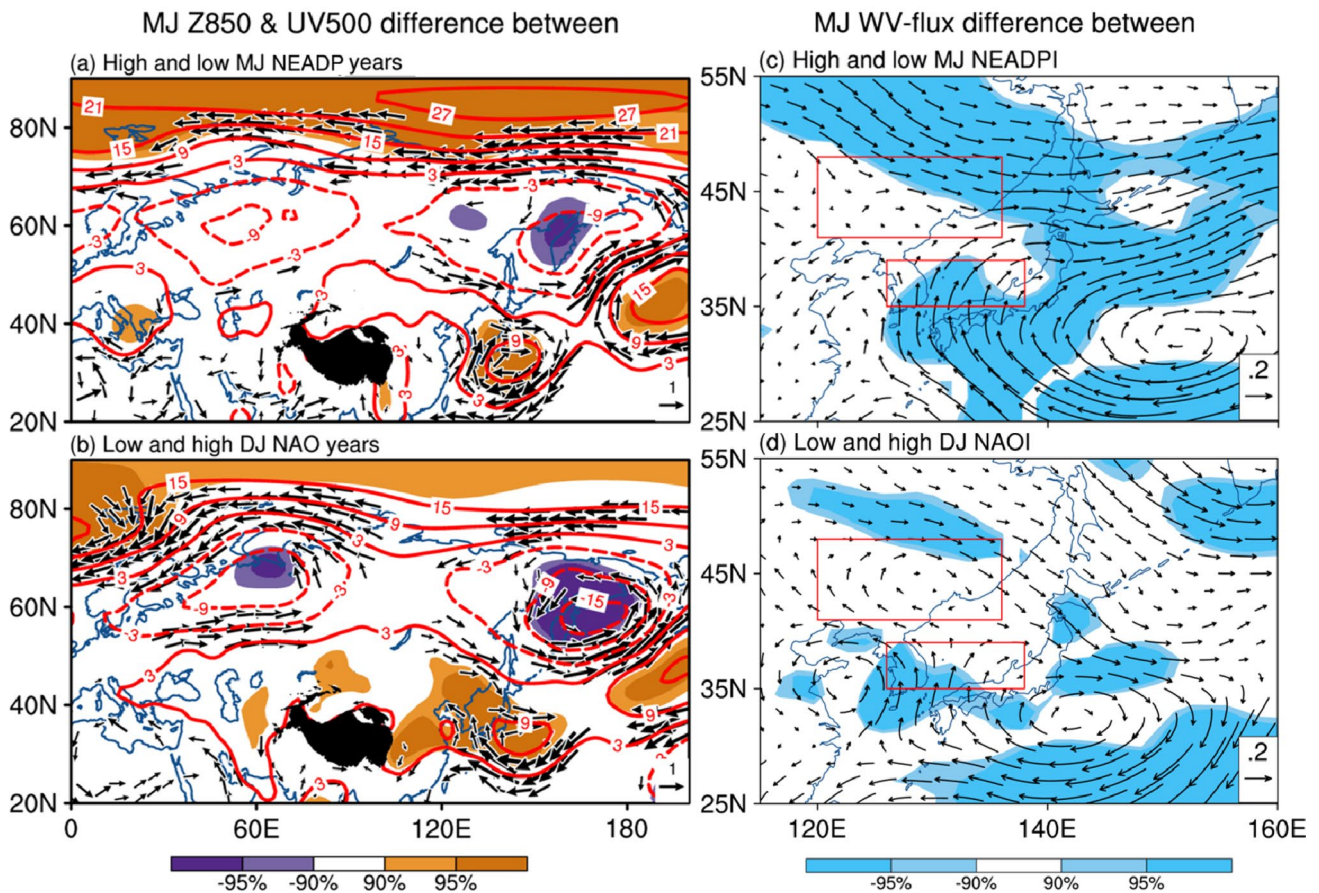
MJ Z850 & UV500 difference between

MJ WV-flux difference between

Fig. 3 **a** 850-hPa geopotential height (contours in units of gpm, interval: 6 gpm) and 500-hPa horizontal wind (vectors in units of m/s), **c** vertically integrated water vapor flux (vectors in units of kg/m/s) composite differences between high and low NEADP indices. **b**, **d** The same as **a**, **c** except for low minus high DJ NAO years. The vectors in **a**, **b** indicate significant values exceeding the 95% confidence level. The dark (light) shadings indicate significant values exceeding the 95% (90%) confidence level. The boxes in the **c**, **d** indicate the regions where NEADPI defined

4 Capacitor effect of Arctic sea ice

a. The Barents sea ice connect winter NAO and NEA summer rainfall.

Many studies have paid high attention to the connection between NAO and Arctic sea ice in the wintertime (Close et al. 2017; Deser et al. 2000; Park et al. 2015; Rothrock and Zhang 2005; Strong et al. 2009; Wu and Wang 2020). For instance, observational and numerical evidence proved that the positive NAO normally transports the moist and warm air from the Atlantic Ocean to the Barents Sea, leading to the melt of the local sea ice (Liu et al. 2004; Wang et al. 2004; Koenigk et al. 2009). In this light, Fig. 5 shows the lead-lad composite of SIC and surface air temperature (SAT) between low and high DJ NAO index. During November, less sea ice and warmer than normal conditions control the Barents sea (Fig. 5a, d). However, such conditions are reversed in the early winter (Fig. 5b, e) and beef up in the late winter (Fig. 5c, f). Figure 6 compares the 1000-hPa geopotential height, horizontal wind, SAT advection, and heat flux (latent plus sensible heat flux) anomalies between low and high DJ NAO index for the early and late winter. The Z1000 pattern displays a seesaw mode with the significant positive and negative centers locating over Iceland and the Azores Islands (Fig. 6a), reflecting a typical negative phase of NAO featured by increased anomalous northerly over the Barents Sea. In this way, the advection of cold air from the north to the Barents Sea would be enhanced (Fig. 6b). The cold SAT together with the increased abnormal northernly over the Barents Sea accelerates the formation of Barents sea ice during winter (Fig. 5b). And accompanied by change of the seawater phase to the sea ice, a large amount of heat flux was released from the ocean to the air (Fig. 6c). However, owing to the much weaker negative phase of the NAO signal during November, the abnormal northerly, cold advection and heat flux releasing cannot be detected over the Barents Sea (Fig. 6d, e, f). Therefore, DJ is the key season for sea ice
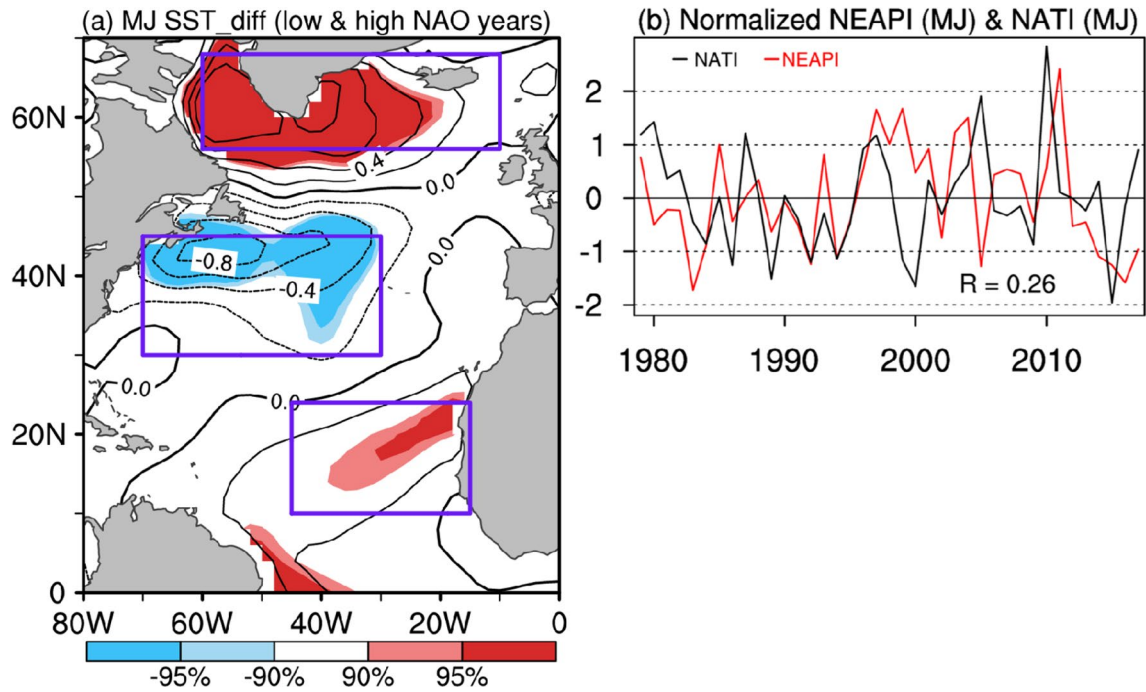
Fig. 4 a MJ sea surface temperature (SST, contours in units of K, interval: 0.2 K) composite difference between low and high DJ NAO indices. The dark (light) shadings indicate significant values exceed-ing the 95% (90%) confidence level. **b** Time series of the normal-ized MJ North Atlantic tripolar SST index (black curve, NATI) and NEADPI (red curve) for the period of 1979–2017
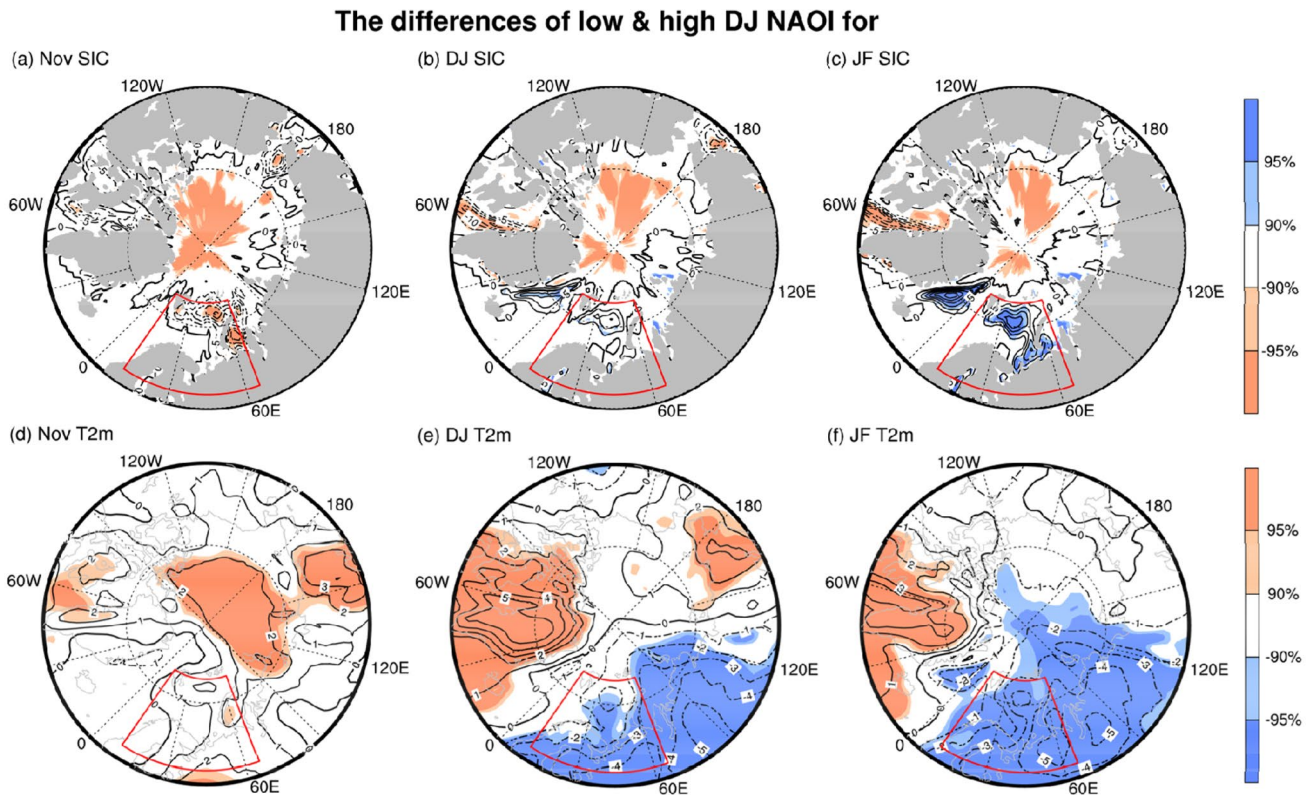

Fig. 5 a November, **b** DJ, **c** JF sea ice concentration (contours in units of %, interval: 5%) composite differences between low and high DJ NAO index. **d–f** Same as **a–c** except for sueface air temperature (contours in units of °C, interval: 1 °C). The dark (light) shadings indicate significant values exceeding the 95% (90%) confidence level
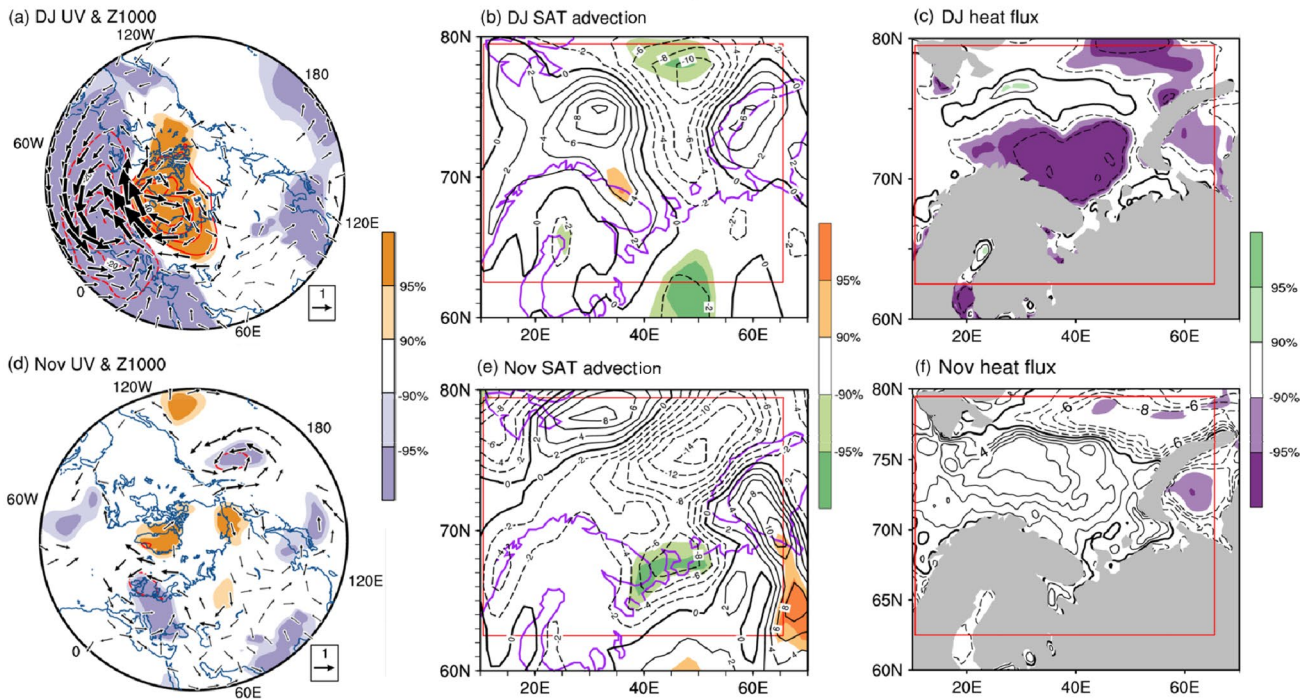
The differences of low & high DJ NAOI for

Fig. 6 The differences of DJ **a** 1000-hPa geopotential (contours in units of gpm, interval: 10 gpm) and horizontal wind (vectors in units of m/s), **b** SAT advection (shadings in units of 10^{-5} °C s^{-1}, interval: 2 10^{-5} °C s^{-1}), **c** heat flux (sensitive plus latent heat flux) anomalies between low and high DJ NAO index. The vectors indicate significant values exceeding the 95% confidence level. The dark (light) shadings indicate significant values exceeding the 95% (90%) confidence level

formation, which is initiated by the enhanced negative NAO signal. And this feature is reminiscent of the effect of anomalous Barents sea ice on the remote atmospheric circulation as revealed by Wu et al. (2016), who found the anomalous Barents sea ice sustains from winter through early spring that triggers a Eurasian Rossby wave train, modifying the precipitation over southern China. In addition to the contribution to the EA spring rainfall, we would like to discuss the potential effect of Arctic sea ice on the linkage between DJ NAO and MJ NEADP.

Figure 7 presents the spring and summer climatology and standard deviation (STD) characteristics of Arctic sea ice in 1979–2017. During the early spring and early summer, large amounts of sea ice cover much of the surface of the Arctic Sea (Fig. 6a, b). For the interannual variability of sea ice, high STD values persist from FMA to MJ in the Barents Sea (Fig. 7c, d). To check the potential coupling connection between the spring Barents sea ice and early summer NEA precipitation, Fig. 8 displays the leading SVD modes of FMA Arctic sea ice anomalies (60°–90° N, 0°–360°) and MJ precipitation anomalies over NEA (35°–55° N, 115°–145° E). The first mode explains 57% of the total squared covariance. The Arctic sea ice pattern for homogeneous correlation is featured by a mono-sign positive anomaly in the Barents Sea and to the east of Greenland

(left panels in Fig. 7a). Its heterogeneous counterpart is also highly correlated with the Barents sea ice. But the positive correlations to the east of Greenland cannot be found. The corresponding precipitation anomaly shows a south-north "seesaw" pattern (right panels in Fig. 8a, b) with positive correlations in Japan and Korean Peninsula and negative correlations in the northeastern Asian continent, which is similar to the DJ NAO-related NEA early summer rainfall pattern (Fig. 2a).

If calculating the composite difference SIC from early spring to early summer between low and high DJ NAO indices, an obvious characteristic is that following the negative DJ NAO, a notable positive SIC anomaly emerges in the Barents Sea in FMA and MJ (Fig. 9a, b). The intensity of anomalous Barents sea ice associated with DJ NAO is stronger in FMA than in JF and MJ (Figs. 5c, 6a, b). We define the sea ice concentration averaged within the region of (62.5°–79.5° N, 10.5°–65.5° E, the boxed region in Fig. 9), where the notable year-to-year variations are excited, as the Barents sea ice index (BSII) to quantitatively scale the variation of the Barents sea ice. The TCC between FMA BSII and the preceding DJ NAO index is −0.49, while that between FMA BSII and MJ NEADPI is 0.56, both exceeding the 99% confidence level.
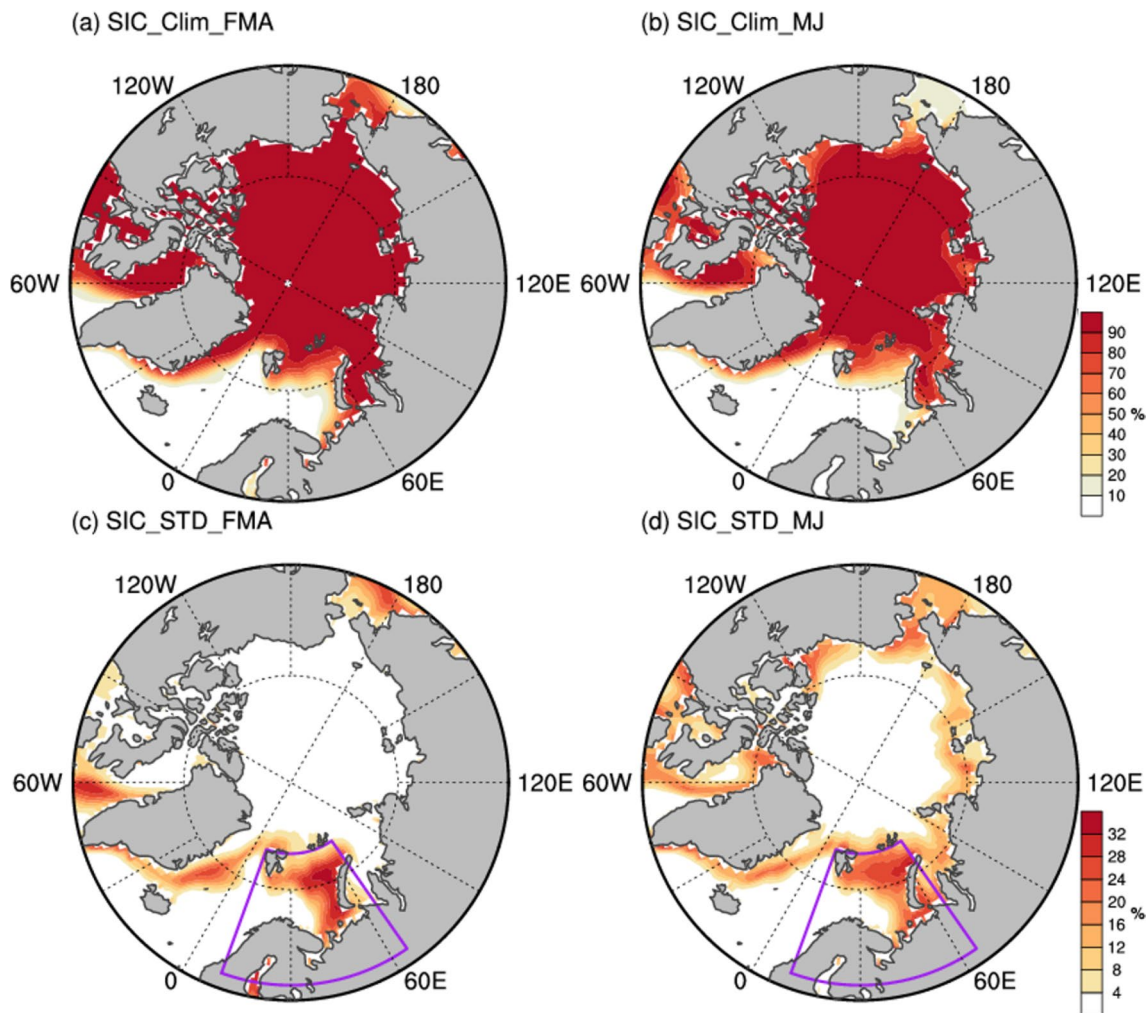
Fig. 7 Climatology of sea ice concentration (shadings in units of %, interval: 10%) in the Arctic region for **a** FMA and **b** MJ. **c, d** The same as **a, b** except for standard deviation (interval: 4%). The purple fan-shaped box indicates the Barents Sea region (62.5°–79.5° N, 10.5°–60.5° E)

How can DJ NAO affect the Barents sea ice in the subsequent seasons? It is known that the switch of the NAO phase corresponds to the equatorward or poleward move of the Atlantic storm track (Trenberth et al. 2005). Taking the negative NAO phase as an example, an enhanced jet stream along 40° N tends to induce cold SST anomalies via accelerating the underlying sea surface latent heat release. In contrast, the low-speed wind prevailing in the areas north of 45° N and south of 30° N decreases the surface latent heat exchange. In consequence, a tripole SSTA pattern appears in response to such NAO-related surface wind anomalies and feeds back to the atmosphere, maintaining the negative phase of NAO during winter (Watanabe et al. 1999; Pan 2005). Wu et al. (2009a, b, their Fig. 6) further noted that this positive ocean–air feedback starts in winter and persists to the consequent spring, but vanishes during the summertime.

Although this positive feedback process maintains the NAO signal from winter to spring, it is unclear whether spring NAO can also exert its forcing effect onto Barents sea ice or not. To clarify the relevant mechanism, the FMA BSII is taken as a reference to calculate the lead-lag regression with 1000-hPa geopotential and horizontal wind (Z/UV1000) (Fig. 10). The regressed 1000-hPa geopotential and horizontal wind fields from a −2-month to a 0-month lead (Fig. 10a–c) displays a spatial distribution that highly resembles the negative NAO, implying that a negative NAO-like pattern is forcing and inducing the increase of Barents sea ice. This reflects a situation similar to that in winter (Koenigk et al. 2009). Nevertheless, the NAO-like pattern disappears in a 1-month and a 2-month lead (Fig. 10d, e), indicating that the effect of anomalous Barents sea ice may not feedback on the persistence of the summer NAO-like anomalies. It also implies that other mechanisms may be responsible for the extensive Barents sea ice during early summer.
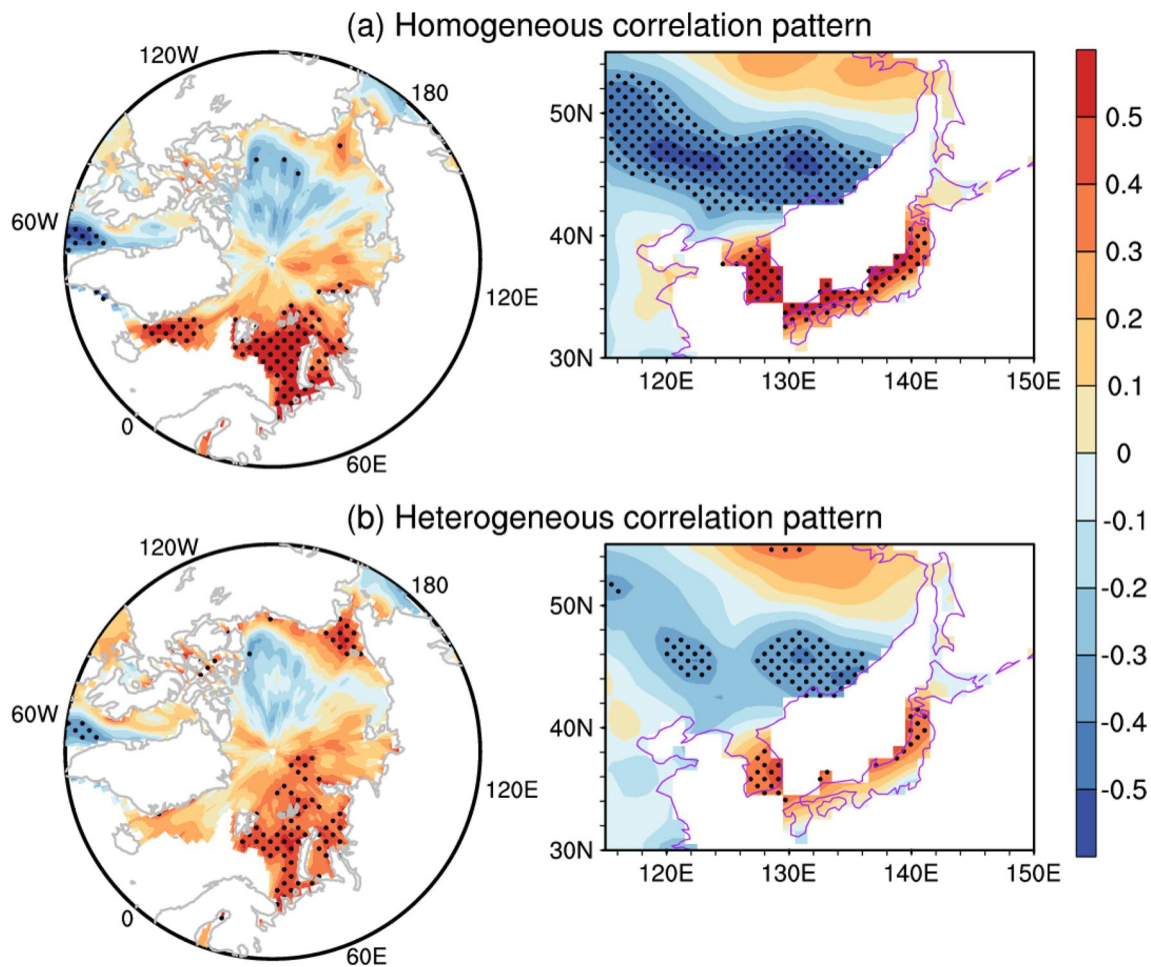
Fig. 8 The first SVD mode for the FMA sea ice anomalies (left panels) in the Arctic (60°–90° N, 0°–360°) and the precipitation anomalies (right panels) during MJ over the NEA area (115°–145° N, 30°–55° E). The shading interval is 0.1. **a, b** The homogeneous and heterogeneous correlation patterns respectively. The dots areas indicate correlation coefficients exceeding the 95% confidence level. The correlation coefficient of the corresponding time series is 0.6

To examine the potential process, we use FMA BSII regressed onto the FMA, MAM, and MJ net radiation fields, respectively. The net radiation is calculated as:

$$\text{Rad}_{net} = \text{DSWRF} + \text{DLWRF} - \text{USWRF} - \text{ULWRF}, \quad (1)$$

where Rad_{net} means net radiation, DSWRF (USWRF), and DLWRF (ULWRF) represent downward (upward) solar radiation and longwave radiation fluxes, respectively. The obvious negative net radiation anomalies can be seen in the Barents Sea (red box) from FMA to MJ (Fig. 11), suggesting that excessive early spring sea ice reduces open water and enhances the sea ice albedo. Strong sea ice albedo reflects more solar radiation and decreases the ice melt, favoring the persistence of SIC anomalies in the Barents Sea from FMA to MJ. This thermodynamic process at the ice-ocean surface has been discussed by Zhang et al. (2000). Here, another

question is proposed that whether Barents sea ice can further impact NEA early summer rainfall.

Figure 12a shows the time series of the normalized FMA and MJ BSII for the past 39 winters (1979–2017). The correlation coefficient between these two indices is 0.87, implying a strong persistence of BSI. If springs (ensuing early summers) with a BSII value [black (red) curves in Fig. 12a for > 0.5 or < 0.5] are considered to be anomalous, there are five high-BSII years (1987, 1998, 2003, 2011, and 2017) and seven low-BSII years (1983, 1984, 1989, 1992, 2002, 2012 and 2013). Note that we choose 0.5 standard deviation as a threshold for spring (early summer) BSII just to obtain the years of remarkably persistent BSI anomaly for the following composite analysis.

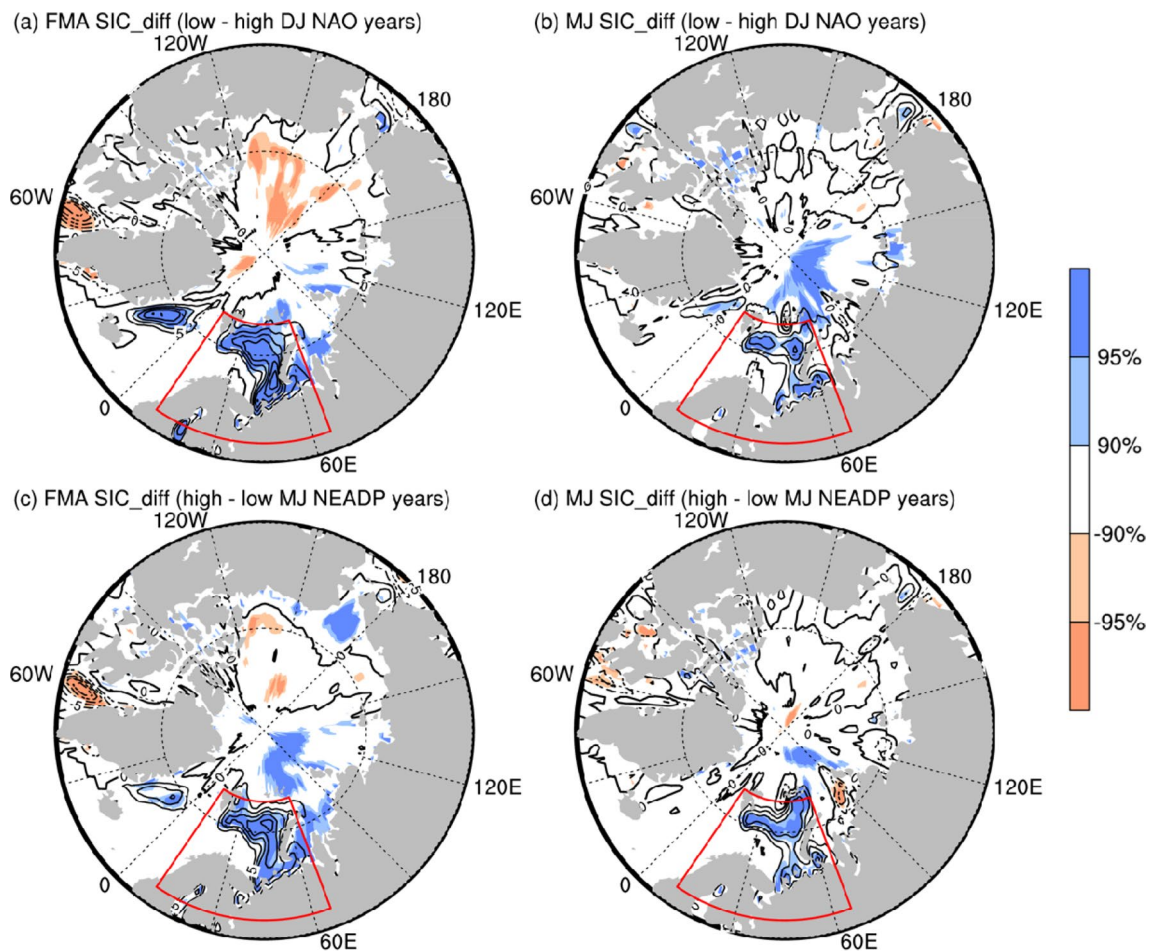b. How Barents sea ice impact NEA summer rainfall?

Fig. 9 **a** FMA, **b** MJ sea ice (shadings in units of %, interval: 5%) difference between low and high DJ NAO indices. **c**, **d** The same as **a**, **b** except for high minus low MJ NEADP years. The dark (light) shadings indicate significant values exceeding the 95% (90%) confidence level. The boxed region indicates the Barents Sea

Figures 13 and 14 show the composite large-scale circulation differences corresponding to the persistent BSI years. The SAT anomalies between high and low BSII show the significant negative anomalies controlling the Barents Sea and eastern Siberia (Fig. 13a). The U500 anomalies associated with extensive BSI exhibit a negative–positive–negative structure over Eurasia (Fig. 13b). In the polar region, salient negative anomalies indicate a decreased circumpolar westerly. Significant positive anomalies elongate from western Europe to East Asia, indicating an enhanced mid-latitude jet. Meanwhile, the subtropical North Pacific is covered by an anomalous negative U500. The composite geopotential anomalies show the spatial pattern resembling Fig. 3, significant negative and positive Z850 anomalies associated with anomalous cyclonic and anticyclonic UV500 locate over the Kamchatka and southern Japan (Fig. 14a). Southeasterly anomalies on the south side of anomalous XWP anticyclone enhance the inflow intensity of moist flux which provides the abundance of vapor to Japan and Korea. Nevertheless,

the westerly anomalies to the south edge of abnormal Kamchatka cyclone tend to limit water vapor conveyance from the Pacific (Fig. 14b). Figure 14c shows that there is a convergence centered over Korea and southern Japan, a divergence located over the NEA continent. The above circulation anomalies jointly contribute to the precipitation pattern over the NEA (Fig. 12b).

However, simultaneous composites do not warrant the potential causality. To further illustrate the impacts of the abnormal BSII-type forcing, we carried out numerical experiments with the ECHAM5.4 model introduced in Sect. 2. The MJ SST and sea ice anomalies associated with persistent BSI anomalies in the Barents Sea (62°–79° N, 10°–65° E) are imposed in the early summer (MJ) climatology fields. Inspecting the differentials of sensitivity and control experiments, the simulated abnormal SAT, U500, UV500, and Z850 are presented in Fig. 15. For the SAT difference between sensitivity and control experiments (Fig. 15a), the salient negative anomalies appear over the Barents Sea, but
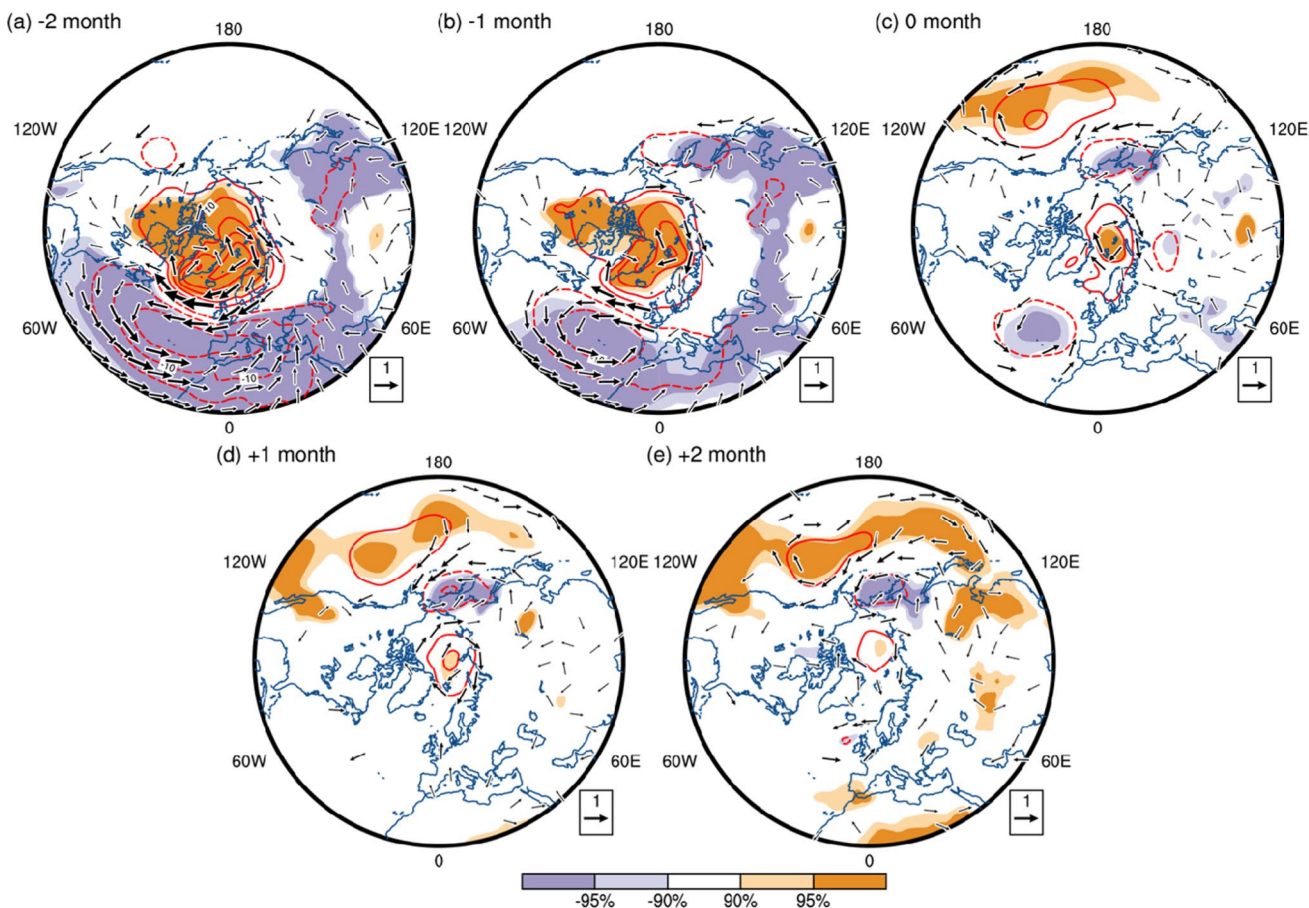
Fig. 10 The lead-lag correlation patterns between the 1000-hPa geopotential (contours in units of gpm, interval: 5 gpm) and horizontal wind (vectors in units of m/s) (UV/Z1000) and the early spring BSII. The BSII leads the UV/Z1000 by **a** −2, **b** −1, **c** 0, **d** +1, and **e** +2 months. The dark (light) shadings and vectors indicate significant values exceeding the 95% (90%) confidence level. Note that −2 months correspond to December–January–February, −1 month correspond to January–February–March, and so on

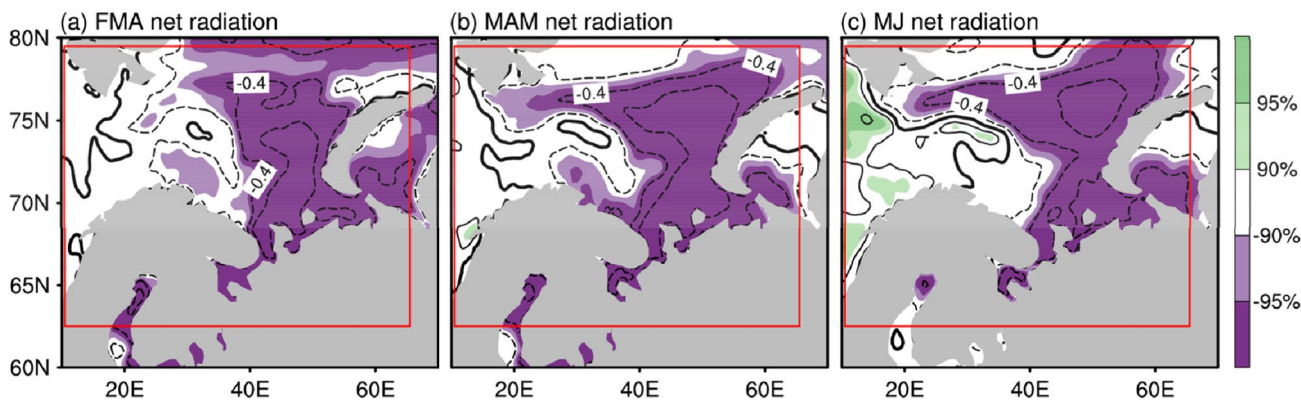**Fig. 11** Linear regressions of **a** FMA, **b** MAM, and **c** MJ net radiation (shadings in units of W/m², interval: 0.2 W/m²) anomalies against FMA BSII. The dark (light) shadings indicate significant values exceeding the (95%) 90% confidence level
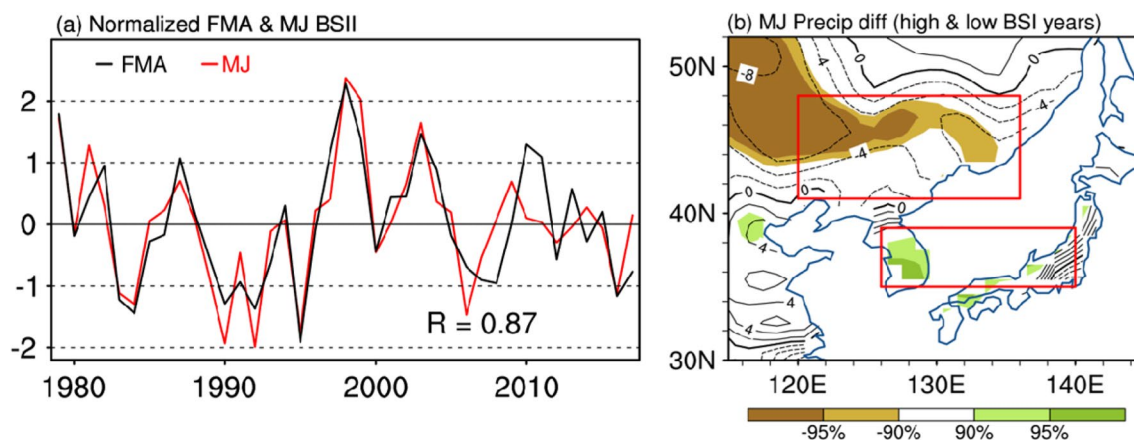
Fig. 12 **a** Time series of the normalized FMA (black) and MJ (red) BSI index for the period of 1979–2017. **b** The MJ precipitation difference between high and low BSI index. The dark (light) shadings indicate significant values exceeding the 95% (90%) confidence level
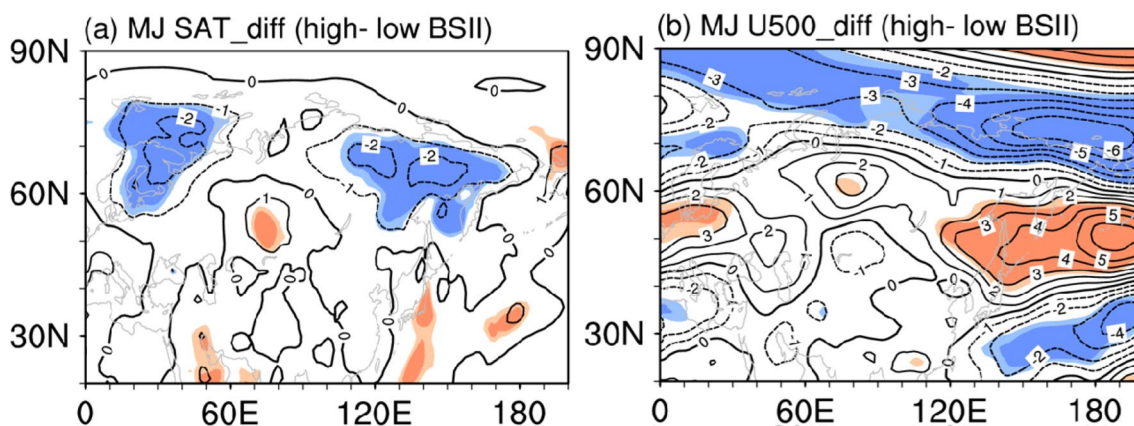

Fig. 13 **a** MJ SAT (°C, interval: 1 °C), **b** MJ U500 (m/s, interval: 1 m/s) difference between high and low persistent BSI years. The dark (light) shadings indicate significant values exceeding the 95% (90%) confidence level

cannot be detected over eastern Siberia comparing with that of the observation (Fig. 13a). A "−, +, −" structure can also be found in the simulated anomalous U500 field except for the northward shift of the mid-latitude jet stream over western Europe (Fig. 15b). For UV/Z500 difference (Fig. 15c), an anomalous high with the anticyclone UV500 anomalies controls the Arctic region. In the mid- to low-latitude regions, the anomalous low and high with the cyclone and anticyclone UV500 anomalies are centered over the Kamchatka and North Pacific. In general, this spatial pattern highly resembles that of the observational result except for the anomalies over the western Eurasia continent (Fig. 14a). For the numerical result, a salient anomalous high accompanied by an abnormal low appears in the western Eurasia continent. For the observational result, the western Eurasian continent is mainly controlled by an obvious low. The reason calls for further study. Figure 15d shows the differences of divergence at 700 hPa and vertically integral of moisture

flux. The abnormal southward moisture flux prevails over Korea and southern Japan, accompanied by the abnormal negative divergence at the lower troposphere. However, the eastward moisture flux along 45° N in Fig. 14c cannot be detected in Fig. 15d. Meanwhile, the abnormal positive divergence sits over the NEA continent. Such anomalous patterns are consistent with the observation results to some extent (Fig. 14c).

Combined with the results of observational analysis and numerical test, the "capacitor" effect of Barents sea ice can be concluded as follows: via the positive feedback between NAO and NAT SSTA from winter to the following early spring (FMA), a negative phase of NAO can be sustained, which increases the simultaneous Barents sea ice. After early spring, an ocean-ice thermodynamic process, maintains the extensive Barents sea ice to early summer. Namely, the extensive sea ice in FMA, which reflects more solar radiation to the air, tends to decrease the absorption of downward
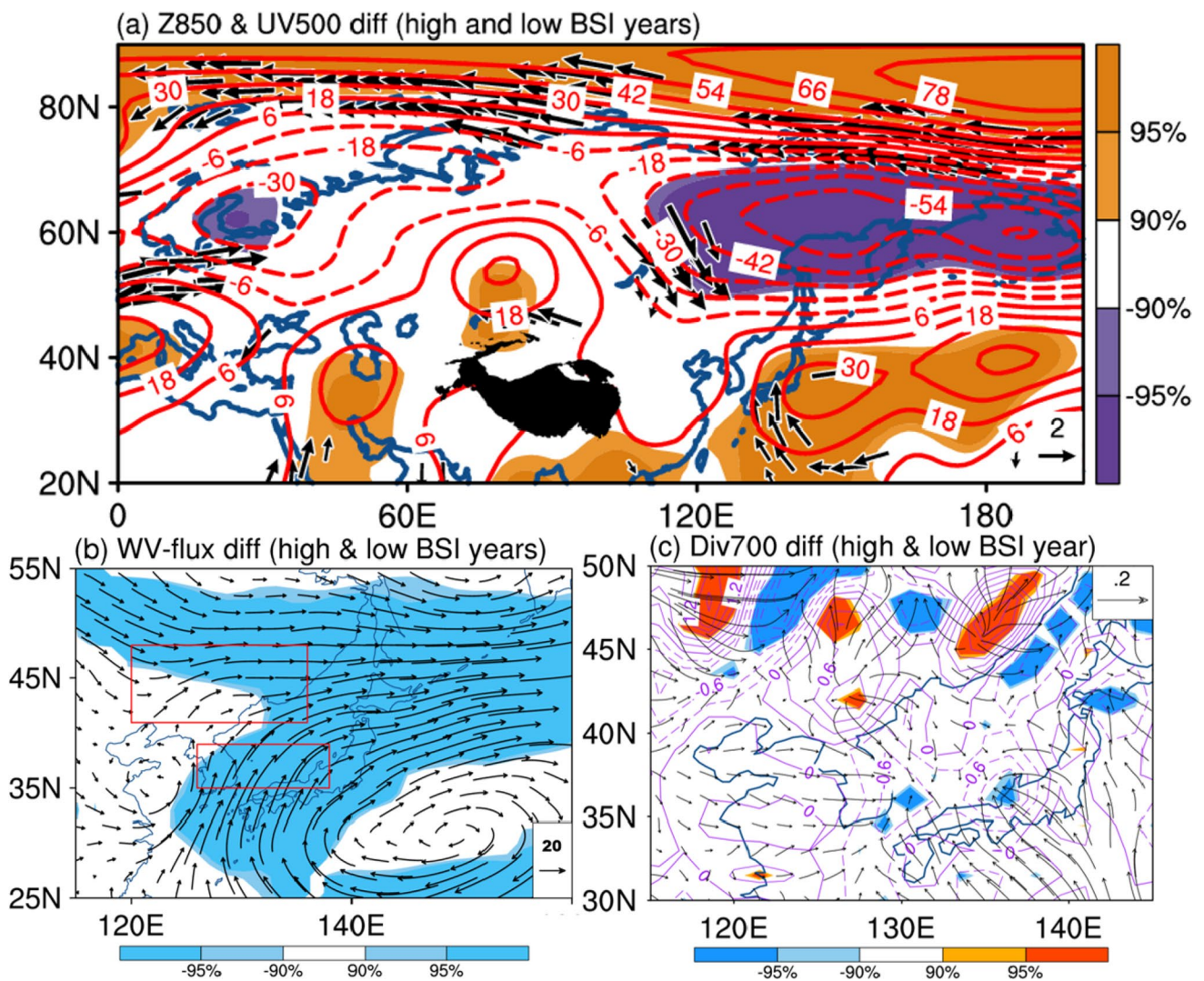
Fig. 14 The same as Fig. 13, except for **a** Z850 and UV500, **b** vertically integrated water vapor flux, **c** divergence (contours in the units of 1/s, interval: 0.3 1/s) and divergent winds (vectors in the units of m/s) at 700-hPa. The dark (light) shadings indicate significant values exceeding the 95% (90%) confidence level

radiation, declining the melting of the summer sea ice. During the early summer, the extensive Barents sea ice tends to reflect more downward solar radiation to the air, inducing a cold local SAT. The accumulation of cold air mass produces favorable effects on the enhancement of anomalous cyclones over the White Sea. The anomalous easterlies (westerlies) along the north (south) flank of this anomalous cyclone may suppress (enhance) the downstream circumpolar westerlies (Eurasian mid-latitude jet stream). Along the enhanced mid-latitude jet stream waveguide, some of the perturbation which is induced by the extensive Barents sea ice may propagate zonally eastward to the downstream regions and contribute to the "positive–negative–positive" geopotential height anomalies occupying the Arctic, eastern Siberia, and XWP. The southeasterly anomalies on the west side of the abnormal XWP anticyclone bring sufficient moisture to Korea and Southern Japan. However, the abnormal northwesterly along the east flank of the abnormal Kamchatka cyclone restricts the Pacific moisture transportation. Accompanying with the negative and positive divergence over the Japan sea and NEA continent, a distinct dipolar precipitation pattern appears over the NEA region during early summer.

5 Empirical prediction of NEADP

In recent decades, despite the rapid development of dynamical climate models, seasonal forecast models still have poor prediction skills for the summer rainfall over East Asia (Wang et al. 2009; Zhao et al. 2020a, b).
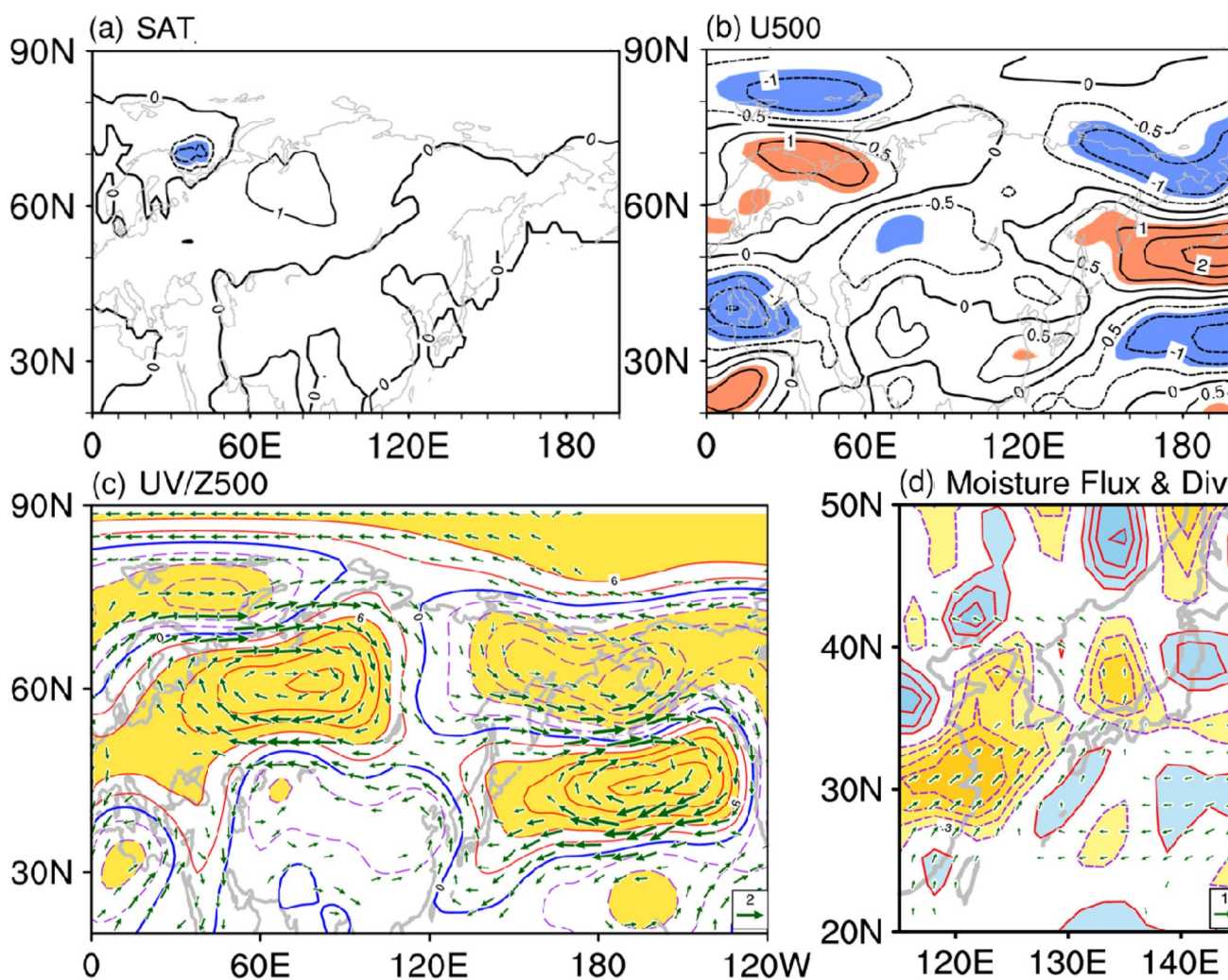
Fig. 15 The ECHAM5 results simulated by BSII-associated MJ Barents Sea SST and SIC anomalies forcing. **a** SAT (contours in units of °C, interval: 1 °C), **b** 500-hPa zonal wind (vectors in units of m/s), **c** 500-hPa horizontal wind and geopotential height (contours in units of gpm, interval: 10 gpm) anomalies. The shaded areas in **a**, **b** imply abnormal values above 1 °C (m/s) or below −1 °C (m/s), in **c** imply abnormal values above 20 gpm or below −20 gpm. **d** 700-hPa divergence (contours and shadings in units of 1/s, interval: 0.3 1/s), and divergent winds (vectors in units of m/s). The vectors indicate anomalous values above 0.5 m/s or below −0.5 m/s

Considering the intimate connection between DJ NAO and MJ dipolar precipitation mode in the NEA, a statistical prediction model is established by a linear regression approach using DJ NAOI for 1979–2017 to examine the contribution of the preceding NAO signal to the predicting skill of the MJ dipolar NEAP. The leave-ten-out cross-validation method is applied to inspect the predictive performance of the empirical model (EPM). The cross-validation method appropriate chooses 30 (29) years from 1979 to 2017 to train the prediction model, and exams it with the residual 10 years. The leaving out ten is according to the conclusion of Blockeel and Struyf (2002), who believed randomly selecting 70–80% of the data to be the training set for conducting regression and the rest as in a test data would avoid overfitting and wasting data. In this study, 75% of the entire period (39 years) roughly equals 30. That's why we choose the leave-ten-out strategy. The correlation coefficient of the observation and prediction indices is calculated as the skill score to access the model performance.

Figure 16a presents the cross-validated estimates of the NEADP. The TCC between the 39-year cross-validated estimates of the EPM based on NAOI and the observed NEADP index is 0.47. Owing to DJ NAOI highly coupled with the simultaneous NAT SSTA, the DJ NATI is also applied to establish the EPM. However, its predict skill (0.27) is much lower than that of DJ NAOI. Figure 16b further shows the spatial pattern between estimates of the empirical model (based on NAOI) and MJ precipitation anomalies in the NEA region. An obvious dipolar pattern controls the NEA,
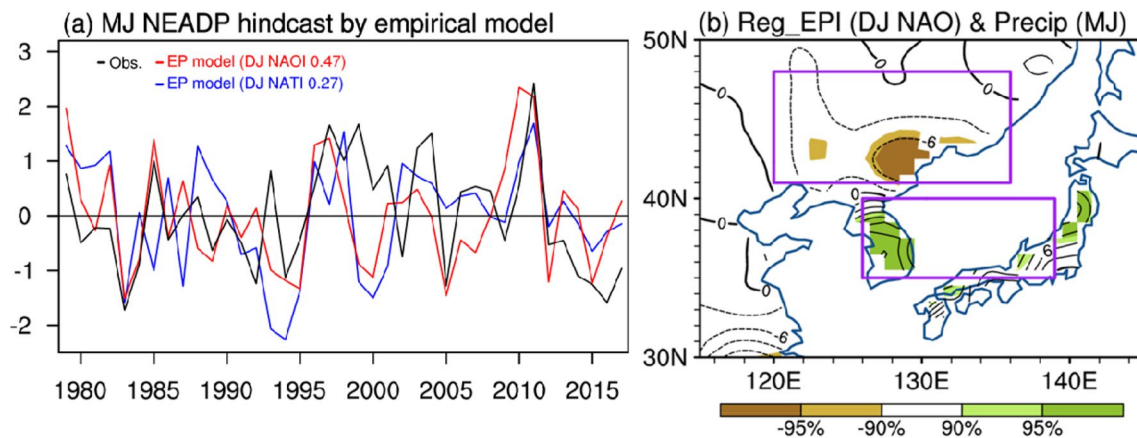
Fig. 16 a The hindcast MJ NEADP made by the empirical model, the red and blue curves are based on the DJ NAOI and NATI, respectively. **b** Regression map of precipitation anomaly over the NEA region against the DJ NAOI-based empirical prediction index. The dark (light) indicate significant values exceeding the 95% (90%) confidence level

indicating the DJ NAO signal can validly predict NEADP about a season in advance.

6 Conclusion and discussion

Northeast Asian early summer rainfall is a critical factor that impacts the local agricultural production. Previous studies have found several factors, including ENSO, the Tibetan Plateau snow cover, Indian Ocean Dipole, Southern Annular Mode, West Pacific subtropical high, and many others (Xiao et al. 2002; Wu et al. 2012a, b; Cao et al. 2014, 2017, 2018; Yang et al. 2017) that influence the summer rainfall in the EA region. However, a relatively small amount of studies focused on the Arctic sea ice, besides, the related physical mechanisms remain debatable and call for more research.

In this article, we contrasted the potential roles of the Barents sea ice and the NAT SSTA in connecting DJ NAO signal and NEA early summer precipitation anomalies. It is found that via the positive feedback between NAO and NAT SSTA from winter to the following early spring (FMA), a negative phase of NAO can be sustained, which increases the simultaneous Barents sea ice. During the early spring, the extensive sea ice reflects more solar radiation to the air and decreases the absorption of downward radiation and the melting of the summer sea ice. Observational and numerical evidence imply that the abnormal positive Barents sea ice, which persist from spring to the early summer, contribute to the "positive–negative–positive" geopotential anomalies pattern occupying the Artic, eastern Siberia, and West Pacific. The southerlies on the west flank of the anomalous XWP high advect plentiful moisture from the Pacific to Korea and southern Japan. A large amount of water vapor concurrent with lower-troposphere convergence increases the local convection and

the early summer rainfall over southern NEA. In contrast, the lower-level divergence induces less precipitation over northern NEA. Through this process, the Barents sea ice acts as a "capacitor" that remembers and extends the winter NAO signal to the ensuing early summer, inducing a dipolar rainfall pattern over the NEA region. And such an anomalous precipitation pattern reflects the second leading mode of MJ precipitation in the NEA.

According to such evidence, we further examine the prospective predictability of the NEADP through building a statistic prediction model in which the anomalous DJ NAO is applied as a predictor. Using the leave-ten-out cross-validation method, the outcome implies that the EPM can skillfully predict the variability of NEA early summer dipolar precipitation by more than a season in advance. The winter NAO, therefore, may offer a predictability source for the NEA early summer rainfall.

Except for SSTA and sea ice anomalies, previous studies also considered the snow cover in the Tibetan Plateau and the mid- to high-latitude Eurasia as the important factors for EA summer monsoon (Wu and Kirtman 2007; Yim et al. 2010; Wu et al. 2012a, b; Xiao and Duan 2016). Therefore, whether DJ NAO can impact NEA early summer rainfall through Eurasian snow cover calls for more studies. Furthermore, with global warming causing frequent extreme rainfall around the world (Donat et al. 2013a, b), what is the realistic scenario for that of NEA? Whether the Arctic sea ice can impact the extreme rainfall over the NEA? These questions are worth further exploring.

References

Barnston AG, Livezey RE (1987) Classification, seasonality and persistence of low–frequency atmospheric circulation patterns. Mon Wea Rev 115:1083–1126

Blockeel H, Struyf J (2002) Efficient algorithms for decision tree cross-validation. J Mach Learn Res 3:621–650

Branstator G (2002) Circumglobal teleconnections, the jet stream waveguide, and the North Atlantic Oscillation. J Clim 15:1893–1910

Bretherton CS, Smith C, Wallace JM (1992) An intercomparison of methods for finding coupled patterns in climate data. J Clim 5:541–560

Brönnimann S (2007) Impact of El Niño–Southern Oscillation on European climate. Rev Geophys 45:RG3003

Cao J, Yao P, Wang L, Liu K (2014) Summer rainfall variability in low-latitude highlands of China and subtropical Indian Ocean Dipole. J Clim 27:880–892

Cao J, Zhang WK, Tao Y (2017) Thermal configuration of the Bay of Bengal–Tibetan Plateau region and the May precipitation anomaly in Yunnan. J Clim 30:9303–9319

Cao J, Ding YC, Wang J, Tao Y (2018) The sea surface temperature configuration of Greenland Sea–subpolar region of North Atlantic and the summer rainfall anomaly in low-latitude highlands of China. Int J Climatol 38:1–8

Chen M, Xie P, Janowiak J, Arkin PA (2002) Global land precipitation: a 50-year analysis based on gauge observations. J Hydrometeorol 3:249–266

Close S, Houssais M, Herbaut C (2017) The Arctic winter sea ice quadrupole revisited. J Clim 30:3157–3167

Dee DP et al (2011) The ERA-Interim reanalysis: configuration and performance of the data assimilation system. Q J R Meteorol Soc 137:553–597

Deser C, Walsh JE, Timlin MS (2000) Arctic sea ice variability in the context of recent atmospheric circulation trends. J Clim 13:617–633

Donat MG, Alexander LV, Yang H, Durre I, Vose R, Caesar J (2013a) Global land-based datasets for monitoring climatic extremes. Bull Am Meteorol Soc 94:997–1006

Donat MG et al (2013b) Updated analyses of temperature and precipitation extreme indices since the beginning of the twentieth century: the HadEX2 dataset. J Geophys Res Atmos 118:2098–2118

Feng J, Li J, Liao H, Zhu JL (2019) Simulated coordinated impacts of the previous autumn North Atlantic Oscillation (NAO) and winter El Niño on winter aerosol concentrations over eastern China. Atmos Chem Phys 19:10787–10800

Gao Z, Hu ZZ, Zhu J, Yang S, Zhang RH, Xiao Z, Jha B (2014) Variability of summer rainfall in Northeast China and its connection with spring rainfall variability in the Huang-Huai region and Indian Ocean SST. J Clim 27:7086–7101

Guo H, Xiao ZN (2019) Decadal variation of rainfall in May over Northeast China since the early 21st century and possible causes. Clim Change Res 15:12–22

Guo D, Gao Y, Bethke I, Gong D, Johannessen OM, Wang H (2014) Mechanism on how the spring arctic sea ice impacts the East Asian summer monsoon. Theor Appl Climatol 115:107–119

Han T, Chen HP, Wang HJ (2015) Recent changes in summer precipitation in Northeast China and the background circulation. Int J Climatol 34:4210–4219

He J, Wu ZW, Jiang Z, Han G (2007) "Climate effect" of the northeast cold vortex and its influences on Meiyu. Sci Bull 51:671–679

He S, Gao Y, Furevik T, Wang H, Li F (2018) Teleconnection between sea ice in the Barents Sea in June and the Silk Road, Pacific-Japan and East Asian rainfall patterns in August. Adv Atmos Sci 35:52–64

Huang B, Thorne PW, Banzon VF, Boyer T, Chepurin G, Lawrimore JH, Menne MJ, Smith TM, Vose RS, Zhang HM (2017) Extended reconstructed sea surface temperature, version 5 (ERSSTv5): upgrades, validations, and intercomparisons. J Clim 30:8179–8205

Hurrell JW (1995) Decadal trends in the North Atlantic Oscillation: regional temperatures and precipitation. Science 269:676–679

Hurrell JW (1996) Influence of variations in extratropical wintertime teleconnections on Northern Hemisphere temperature. Geophys Res Lett 23:665–668

Koenigk T, Mikolajewicz U, Jungclaus JH, Alexandra K (2009) Sea ice in the Barents Sea: seasonal to interannual variability and climate feedbacks in a global coupled model. Clim Dyn 32:1119–1138

Lee E, Jhun J, Park C (2005) Remote connection of the northeast Asian summer rainfall variation revealed by a newly defined monsoon index. J Clim 18:4381–4393

Li J, Wu Z (2012) Importance of autumn Arctic sea ice to northern winter snowfall. PNAS 109:E1898–E1898

Li J, Sun C, Jin FF (2013) NAO implicated as a predictor of Northern Hemisphere mean temperature multidecadal variability. Geophys Res Lett 40:5497–5502

Liu J, Curry JA, Hu Y (2004) Recent Arctic sea ice variability: connection to the Arctic Oscillation and the ENSO. Geophys Res Lett 31:L09211

Liu Y, Zhu Y, Wang H, Gao Y, Sun J, Wang T, Ma J, Yurova A, Li F (2020) Role of autumn Arctic Sea ice in the subsequent summer precipitation variability over East Asia. Int J Climatol 40:706–722

Luo B, Luo D, Wu L, Zhong L, Simmonds I (2017) Atmospheric circulation patterns which promote winter Arctic sea ice decline. Environ Res Lett 12:054017

Pan L (2005) Observed positive feedback between the NAO and the North Atlantic SSTA tripole. Geophys Res Lett 32:L06707

Park H, Lee S, Son S, Feldstein SB, Kosaka Y (2015) The impact of poleward moisture and sensible heat flux on Arctic winter sea ice variability. J Clim 28:5030–5040

Rayner NA, Parkler DE, Horton EB, Folland CK, Alexander LV, Rowell DP, Kent EC, Kaplan A (2003) Global analyses of sea surface temperature, sea ice, and night marine air temperatures since the late nineteenth century. J Geophys Res 108(D14):4407

Roeckner E et al (2003) The atmospheric general circulation model ECHAM5. Part I: model description. Max-Planck Institute Rep. 349

Rothrock DA, Zhang J (2005) Arctic Ocean sea ice volume: what explains its recent depletion? J Geophys Res 110:C01002

Screen JA (2013) Influence of Arctic sea ice on European summer precipitation. Environ Res Lett 8:044015

Shen BZ, Lin ZD, Lu RY, Lian Y (2011) Circulation anomalies associated with interannual variation of early- and late-summer precipitation in Northeast China. Sci China Earth Sci 54:1095–1104

Shukla J (1998) Predictability in the midst of chaos: a scientific basis for climate forecasting. Science 282:728–731

Strong C, Magnusdottir G, Stern H (2009) Observed feedback between winter sea ice and the North Atlantic Oscillation. J Clim 22:6021–6032

Thompson DW, Wallace JM (1998) The Arctic Oscillation signature in the wintertime geopotential height and temperature fields. Geophys Res Lett 25:1297–1300

Thompson DW, Wallace JM (2000) Annular modes in the extratropical circulation. Part I: month-to-month variability. J Clim 13:1000–1016

Trenberth KE, Stepaniak DP, Smith L (2005) Interannual variability of patterns of atmospheric mass distribution. J Clim 18:2812–2825

Wallace JM, Gutzler DS (1981) Teleconnections in the geopotential height field during the Northern Hemisphere winter. Mon Wea Rev 109:784–812

Wang J, Wu B, Tang CCL, Walsh JE, Ikeda M (2004) Seesaw structure of subsurface temperature anomalies between the Barents Sea and the Labrador Sea. Geophys Res Lett 31:L19301

Wang B, Lee JY et al (2009) Advance and prospect of seasonal prediction: assessment of APCC/CliPAS 14-model ensemble retrospective seasonal prediction (1980–2004). Clim Dyn 33:93–117

Watanabe M, Kimoto M, Nitta T (1999) A comparison of decadal climate oscillations in the North Atlantic detected in observations and a coupled GCM. J Clim 12:2920–2940

Wu R, Kirtman BP (2007) Observed relationship of spring and summer East Asian rainfall with winter and spring Eurasian snow. J Clim 20:1285–1304

Wu R, Wang Y (2020) Comparison of North Atlantic Oscillation-related changes in the North Atlantic sea ice and associated surface quantities on different time scales. Int J Climatol 40:2686–2701

Wu J, Wu Z (2019) Interdecadal change of the spring NAO impact on the summer Pamir–Tienshan Snow Cover. Int J Climatol 39:629–642

Wu R, Hu Z-Z, Kirtman BP (2003) Evolution of ENSO-related rainfall anomalies in East Asia. J Clim 16:3742–3758

Wu B, Zhang R, Rosanne D (2008) Arctic dipole anomaly and summer rainfall in Northeast China. Chin Sci Bull 53:2222

Wu B, Zhang R, Wang B, D'Arrigo R (2009a) On the association between spring Arctic sea ice concentration and Chinese summer rainfall. Geophys Res Let 36:L09501

Wu Z, Wang B, Li J, Jin FF (2009b) An empirical seasonal prediction model of the East Asian summer monsoon using ENSO and NAO. J Geophys Res 114:D18120

Wu Z, Li JP, Jiang Z, He J, Zhu X (2012a) Possible effects of the North Atlantic Oscillation on the strengthening relationship between the East Asian summer monsoon and ENSO. Int J Climatol 32:794–800

Wu Z, Li J, Jiang Z, Ma T (2012b) Modulation of the Tibetan Plateau snow cover on the ENSO teleconnections: from the East Asian summer monsoon perspective. J Clim 25:2481–2489

Wu B, Zhang R, D'Arrigo R, Su J (2013) On the relationship between winter sea ice and summer atmospheric circulation over Eurasia. J Clim 26:5523–5536

Wu Z, Li X, Li YJ, Li Y (2016) Potential influence of Arctic sea ice to the inter-annual variations of East Asian spring precipitation. J Clim 29:2797–2813

Xiao Z, Duan A (2016) Impacts of Tibetan Plateau snow cover on the interannual variability of the East Asian summer monsoon. J Clim 29:8495–8514

Xiao Z, Yan H, Li C (2002) Relationship between dipole oscillation of SSTA of Indian Ocean region and precipitation and temperature in China. J Trop Meteorol 2:121–131

Yamamoto K, Tachibana Y, Honda M, Ukita J (2006) Intra-seasonal relationship between the Northern Hemisphere sea ice variability and the North Atlantic Oscillation. Geophys Res Lett 33:L14711

Yang RW, Xie ZA, Cao J (2017) A dynamic index for the westward ridge point variability of the western Pacific subtropical high during summer. J Clim 30:3325–3341

Yim SY, Jhun JG, Lu R, Wang B (2010) Two distinct patterns of spring Eurasian snow cover anomaly and their impacts on the East Asian summer monsoon. J Geophys Res 115:D22113

Yin Z, Yuan D, Zhang X, Yang Q, Xia S (2020) Different contributions of Arctic sea ice anomalies from different regions to North China summer ozone pollution. Int J Climatol 40:559–571

Zhang J, Rothrock D, Steele M (2000) Recent changes in Arctic sea ice: the interplay between ice dynamics and thermodynamics. J Clim 13:3099–3114

Zhang R, Sun C, Zhang R, Jia L, Li W (2018) The impact of Arctic sea ice on the inter-annual variations of summer Ural blocking. Int J Climatol 38:4632–4650

Zhang P, Wang B, Wu Z (2019) Weak El Niño and Winter Climate in the mid-high latitude Eurasia. J Clim 32:402–421

Zhang P, Wu Z, Li J, Xiao Z (2020) Seasonal prediction of the northern and southern temperature modes of the East Asian winter monsoon: the importance of the Arctic sea ice. Clim Dyn. https://doi.org/10.1007/s00382-020-05182-w

Zhao P, Zhang X, Zhou X, Ikeda M, Yin Y (2004) The sea ice extent anomaly in the North Pacific and its impact on the East Asian summer monsoon rainfall. J Clim 17:3434–3447

Zhao J, Zhou J, Xiong K, Feng G (2020a) Relationship between Tropical Indian Ocean SSTA in Spring and precipitation of Northeast China in Late Summer. J Meteorol Res 33:1060–1074

Zhao JH, Xiong KG, Chen LJ (2020b) The reason of low predictive skills of precipitation in flood season in Northeast China. Chin Atmos Sci. https://doi.org/10.3878/j.issn.1006-9895.1911.19132. **(in Chinese)**

Zheng F, Li J, Li YJ, Zhao S, Deng DF (2016) Influence of the summer NAO on the spring–NAO–based predictability of the East Asian summer monsoon. J Appl Meteorol Climatol 55:1459–1476

Zhou J, Zhao J, He W, Gong Z (2015) Spatiotemporal characteristics and water budget of water cycle elements in different seasons in northeast China. Chin Phys B 24:567–574

Zuo J, Li WJ, Sun CH, Xu L, Ren HL (2013) Impact of the North Atlantic sea surface temperature tripole on the East Asian summer monsoon. Adv Atmos Sci 30:1173–1186